SOLAR CELLS

Constructive molecular configurations for surface-defect passivation of perovskite photovoltaics

Rui Wang[1]*, Jingjing Xue[1]*†, Kai-Li Wang[2]*, Zhao-Kui Wang[1,2]†, Yanqi Luo[3], David Fenning[3], Guangwei Xu[1], Selbi Nuryyeva[1,4], Tianyi Huang[1], Yepin Zhao[1], Jonathan Lee Yang[5], Jiahui Zhu[1], Minhuan Wang[1], Shaun Tan[1], Ilhan Yavuz[6]†, Kendall N. Houk[4]†, Yang Yang[1,7]†

Surface trap–mediated nonradiative charge recombination is a major limit to achieving high-efficiency metal-halide perovskite photovoltaics. The ionic character of perovskite lattice has enabled molecular defect passivation approaches through interaction between functional groups and defects. However, a lack of in-depth understanding of how the molecular configuration influences the passivation effectiveness is a challenge to rational molecule design. Here, the chemical environment of a functional group that is activated for defect passivation was systematically investigated with theophylline, caffeine, and theobromine. When N-H and C=O were in an optimal configuration in the molecule, hydrogen-bond formation between N-H and I (iodine) assisted the primary C=O binding with the antisite Pb (lead) defect to maximize surface-defect binding. A stabilized power conversion efficiency of 22.6% of photovoltaic device was demonstrated with theophylline treatment.

Defect passivation to reduce unproductive charge recombination is an effective strategy to increase the power conversion efficiency (PCE) of polycrystalline metal-halide perovskite thin-film photovoltaics (PVs) (*1*–*6*). The ionic nature of the perovskite lattice enables molecular passivation through coordinate binding based on Lewis acid-base chemistry (*7*–*10*). Organic molecules containing various functional groups, such as carbonyl groups, can passivate defects (*11*–*17*). The selection of molecules with optimal binding configurations for defect passivation would benefit from molecular design rules.

We demonstrate high efficiencies for $(FAPbI_3)_x(MAPbBr_3)_{1-x}$ (where FA is formamidinium and MA is methylammonium; x is 0.92 in the precursor) perovskite PV devices through defect identification followed by rational design and comprehensive investigation of the chemical environment around the active functional group for defect passivation (*18*). In high-quality perovskite polycrystalline thin films that have monolayered grains (*19*–*21*), interior defects of perovskite are negligible compared with the surface defects. We used density functional theory (DFT) calculations to compare the formation energies of selected native defects on the perovskite surface. Particularly taken into consideration were Pb- and I-involving point defects, Pb vacancy (V_{Pb}), I vacancy (V_I), and Pb-I antisite (Pb_I and I_{Pb}, corresponding to I site substitution by Pb and Pb site substitution by I, respectively) because the band edges of perovskite were reported to be composed of Pb and I orbitals (*22*, *23*).

As confirmed by x-ray photoelectron spectroscopy (XPS), the surface of the as-fabricated perovskite thin film synthesized by a two-step method was Pb-rich (fig. S1), and we focused on the (100) surface with PbI_2 termination in a Pb-rich condition. The types of surface defects studied and their corresponding top-layer view of atomic structures are shown in Fig. 1A. Using the Dispersion Correction 3 (DFT-D3) method, we calculated the defect formation energies (DFEs) (table S1) of V_{Pb}, V_I, Pb_I, and I_{Pb} on the surface to be 3.20, 0.51, 0.57, and 3.15 eV, respectively. Compared with the values reported in bulk perovskite, V_{Pb}, V_I, and I_{Pb} defects show similar DFEs (*24*), whereas the Pb_I antisite defect exhibited particularly lower formation energy than that in the bulk. Thus, the Pb_I antisite defect should form more readily and predominate on the surface. We did not consider V_I further despite its DFE being as low as that of Pb_I, because the interaction of molecules with the V_I turned out to be not energy favorable (fig. S2).

On the basis of these results, we focused on the interaction between the surface Pb_I antisite defect and candidate molecules for defect passivation. A set of small molecules sharing the identical functional groups but with strategically varying chemical structure were investigated, namely theophylline, caffeine, and theobromine, interacting with the defects (Fig. 1B). These molecules are found in natural

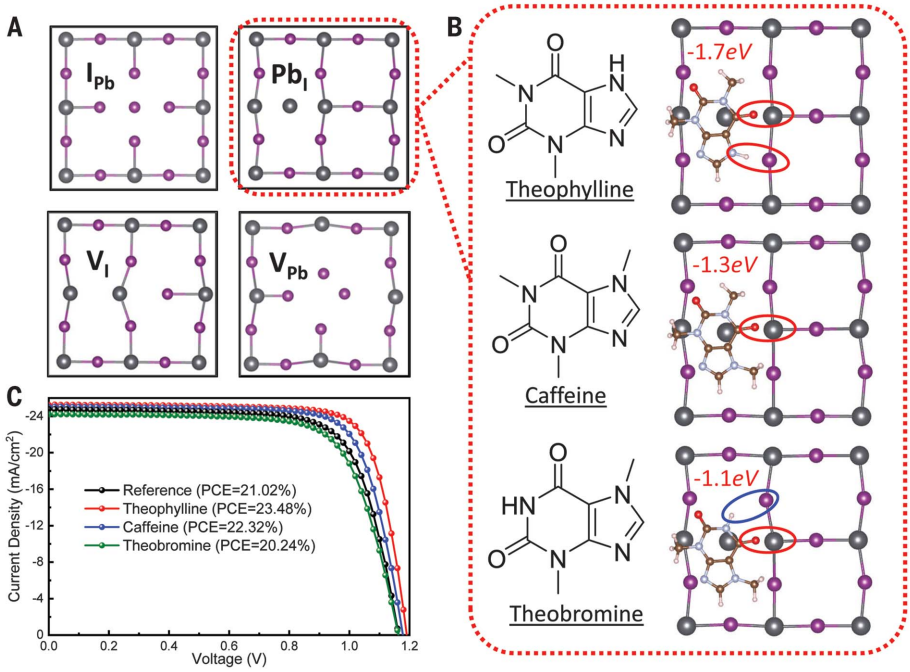

Fig. 1. Surface-defect identification and constructive configuration of the C=O group in three different chemical environments. (**A**) Top view of the various types of surface defects. (**B**) Theoretical models of perovskite with molecular surface passivation of Pb_I antisite with theophylline, caffeine, and theobromine. (**C**) *J-V* curves of perovskite solar cells with or without small-molecules treatment under reverse scan direction.

[1]Department of Materials Science and Engineering and California NanoSystems Institute, University of California Los Angeles, CA 90095, USA. [2]Institute of Functional Nano & Soft Materials (FUNSOM), Jiangsu Key Laboratory for Carbon-Based Functional Materials & Devices, Soochow University, Suzhou 215123, China. [3]Department of Nanoengineering, University of California, San Diego, La Jolla, CA 92093, USA. [4]Department of Chemistry and Biochemistry, University of California Los Angeles, CA 90095, USA. [5]College of Chemistry, University of California Berkeley, CA 94720, USA. [6]Department of Physics, Marmara University, Ziverbey, Istanbul 34722, Turkey. [7]School of Engineering, Westlake University, Hangzhou 310024, China.
*These authors contributed equally to this work.
†Corresponding author. Email: jjxue@ucla.edu (J.X.); zkwang@suda.edu.cn (Z.-K.W.); ilhan.yavuz@marmara.edu.tr (I.Y.); houk@chem.ucla.edu (K.N.H.); yangy@ucla.edu (Y.Y.)

products (tea, coffee, and chocolate, respectively) and are readily accessible. In these molecules, the conjugated structure as well as the dipoles induced by the hetero atoms tend to increase the intermolecular interaction. This renders them nonvolatile in nature, which is key to the investigation of their interactions with defects in perovskite and long-term stability of the devices. The xanthine core also helps maintain the coplanarity of the carbonyl group and the N–H. Unlike other small molecules with flexible alkyl chains, this rigidity allows us to define the configuration and distance between the carbonyl group and N–H when they are interacting with the defects, as a result of which the constructive molecular configuration for defect passivation can be unraveled.

We incorporated theophylline onto the surface of perovskite thin film using a post-treatment method, and a PCE enhancement from 21.02% (stabilized 20.36%) to 23.48% (stabilized 22.64%) was observed in the PV devices with ITO/SnO_2/perovskite/Spiro-OMeTAD/Ag structure under reverse scan direction [where ITO is indium tin oxide, SnO_2 is tin oxide, and Spiro-OMeTAD is 2,2′7,7′-tetrakis-(*N*,*N*-di-*p*-methoxyphenyl amine)-9,9′-spirobifluorene]. Current density-voltage (*J-V*) curves of the PV devices with and without theophylline treatment are compared in Fig. 1C and table S2. The control device showed an open-circuit voltage (V_{OC}) of 1.164 V, a short-circuit current (J_{SC}) of 24.78 mA cm^{-2}, and a fill factor (FF) of 72.88%, whereas the target device showed a V_{OC} of 1.191 V, a J_{SC} of 25.24 mA cm^{-2}, and an FF of 78.11%. The enhancement in the V_{OC} was attributed to the surface passivation by theophylline through the Lewis base-acid interaction between C=O group and the antisite Pb. As shown in the surface structure model of perovskite with theophylline (Fig. 1B), the C=O group on theophylline strongly interacted with the antisite Pb. The neighboring N–H on the imidazole ring also interacted with the I of PbI_6^{2-} octahedron through a hydrogen bond (H-bond), which strengthened the absorption of theophylline onto the Pb_I defect, resulting in an interaction energy (E_{int}, defined as $E_{molecule\text{-}perovskite} - E_{perovskite} - E_{molecule}$) as strong as −1.7 eV.

This observation suggested that the neighboring H-bond between the xanthine molecule and the PbI_6^{2-} octahedron can contribute to the defect passivation. A methyl group was added to the N on the imidazole ring of theophylline (resulting in caffeine) to eliminate the effect from H-bonding between the N–H and I, leaving just the interaction with surface Pb_I defects (Fig. 1B). The missing H-bond between N–H and PbI_6^{2-} octahedron resulted in a weakened interaction and a less favorable E_{int} of −1.3 eV. Compared with the theophylline-treated device, a caffeine-treated perovskite PV device had a lower PCE of 22.32% along with a lower V_{OC} of 1.178 V, J_{SC} of 25.04 mA cm^{-2}, and FF of 75.76%.

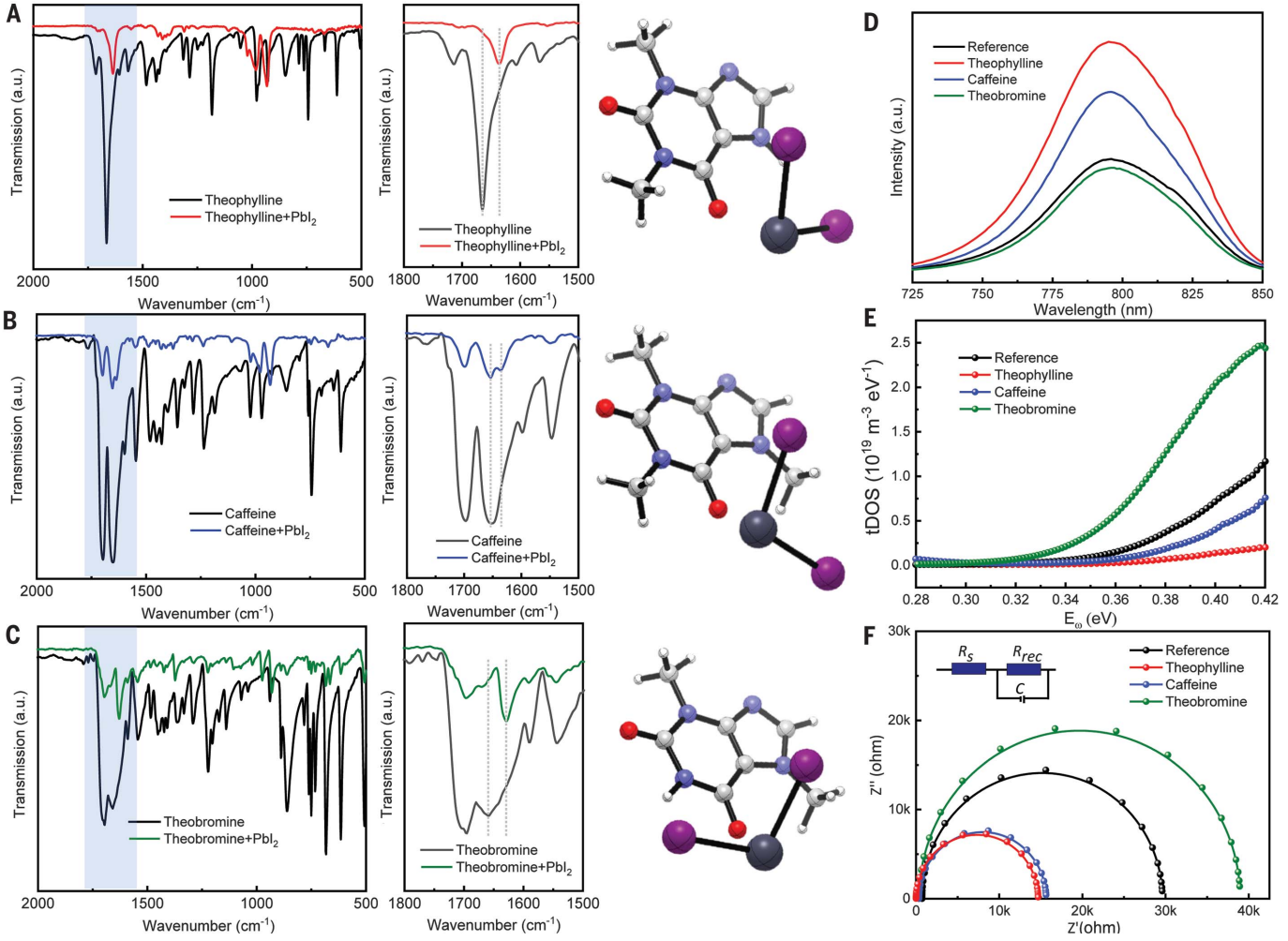

Fig. 2. Investigation of the interactions between surface defects and the small molecules. FTIR spectra of (**A**) pure theophylline and theophylline-PbI_2 films, (**B**) pure caffeine and caffeine-PbI_2 films, and (**C**) pure theobromine and theobromine-PbI_2 films. (**D**) PL spectra of perovskite films without and with small-molecules treatment. (**E**) *t*DOS in perovskite solar cells with or without small-molecules treatment. (**F**) Nyquist plots of perovskite solar cells with or without small-molecules treatment measured in the dark and at corresponding open-circuit voltages. a.u., arbitrary units; *C*, junction capacitance; R_{rec}, recombination resistance; R_s, Series Resistance.

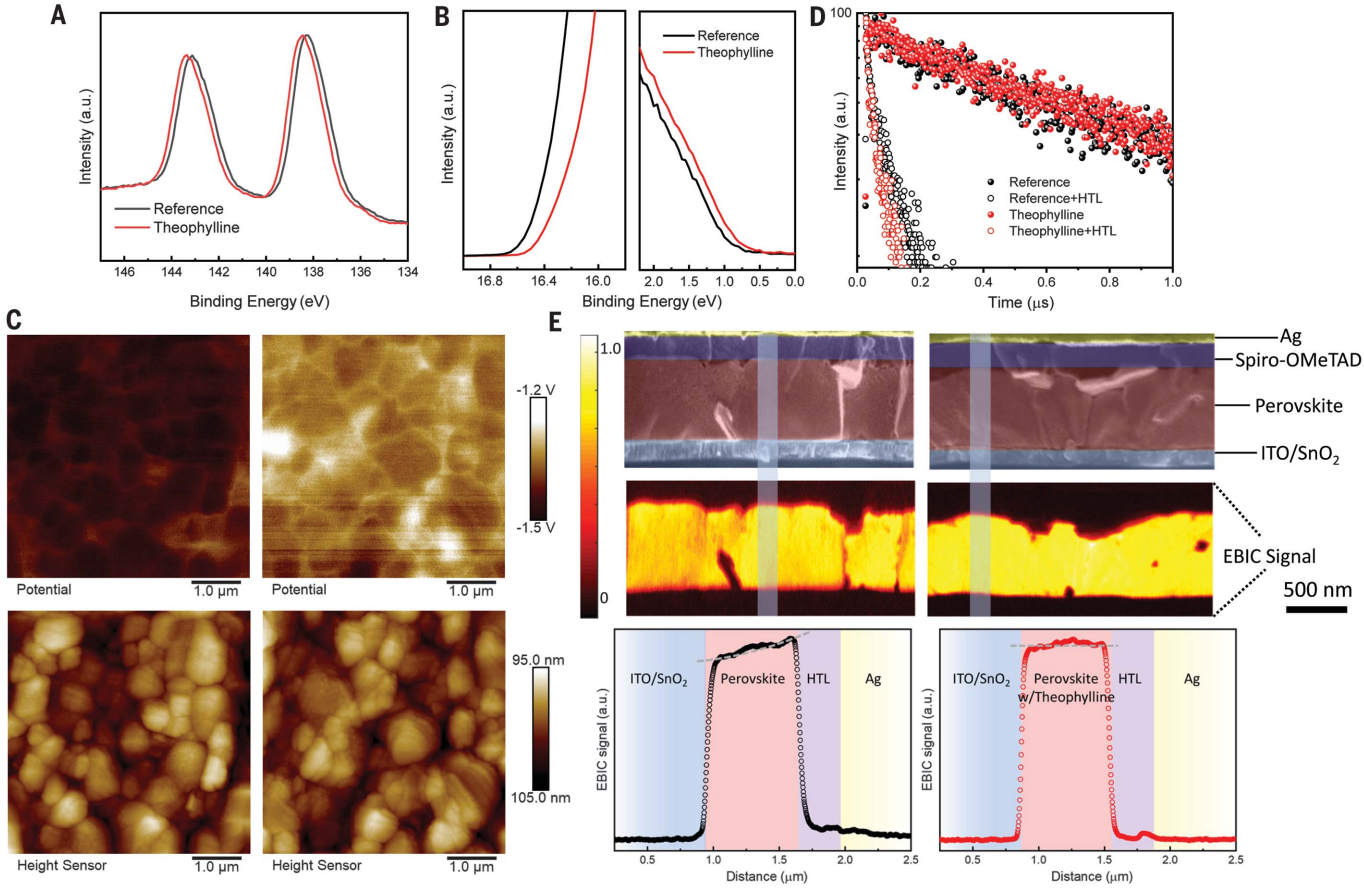

Fig. 3. Characterization of perovskite films and interfaces with theophylline treatment. (**A**) XPS data for Pb 4f 7/2 and Pb 4f 5/2 core-level spectra in perovskite films with or without theophylline treatment. (**B**) UPS spectra of perovskite films with or without theophylline treatment. (**C**) AFM and KPFM images of perovskite films with (right) or without (left) theophylline treatment. (**D**) Time-resolved PL spectra of perovskite films before and after depositing Spiro-OMeTAD without and with theophylline treatment. (**E**) Cross-section SEM images and the corresponding EBIC images and line profile of the perovskite solar cells with (right) or without (left) theophylline treatment.

When the N–H group was located next to the C=O group on the same six-membered ring, producing a shorter distance between the C=O and the N–H, in theobromine, the spatially effective interaction between the N–H and I was disabled as C=O was bound to antisite Pb, resulting in an even weaker E_{int} of −1.1 eV (Fig. 1B). Although C=O and N–H are both present on the molecule, the lack of appropriate coordination of I to the molecule led to a spatially destructive molecular configuration. The theobromine-treated devices showed a decrease in PCE to 20.24% with a lower V_{OC} of 1.163 V, J_{SC} of 24.27 mA cm^{-2}, and FF of 71.58% compared with the reference device. This result emphasizes the importance of the constructive configuration of N–H and C=O groups that enable the cooperative multisite interaction and synergistic passivation effect.

We studied the variation in the C=O and the PbI_2-terminated perovskite surface interaction with different molecular configurations using Fourier-transform infrared spectroscopy (FTIR). The C=O in pure theophylline showed a typical stretching vibration mode at 1660 cm^{-1} that it shifted to 1630 cm^{-1} upon binding to PbI_2 (Fig. 2A). The downward shift of 30 cm^{-1} of the C=O stretching vibration frequency resulted from the electron delocalization in C=O when a Lewis base-acid adduct was formed, demonstrating a strong interaction between PbI_2 and C=O in theophylline. The atomic distance between the O in C=O and the Pb in PbI_2, on the basis of theoretical modeling, was as low as 2.28 Å.

When the H atom was replaced by a methyl group on the N of imidazole to eliminate the effect of an H bond, the vibration frequency of C=O in caffeine shifted only 10 cm^{-1} upon addition of PbI_2, indicating a weakened interaction between the C=O and PbI_2 (Fig. 2B). The atomic distance between the corresponding O and Pb also increased to 2.32 Å. In the case of theobromine, when the N–H was in a closer position to C=O, the interaction between the molecule and PbI_2 became comparable to that in theophylline, as evidenced by the large shift of C=O stretching vibration frequency from 1655 to 1620 cm^{-1} and the short distance between O and Pb (Fig. 2C). However, this strong interaction was enabled by the free rotation of PbI_2, which resulted in a different configuration than that in theophylline and caffeine. Hence, when the configuration of PbI_2 was fixed and had a 90° angle between Pb and I atom, like that on perovskite surface (the PbI_6^{2-} octahedron), the N–H was in a position that led to an unfavorable interaction with I. This configuration would cause either weakened interaction between the molecule and the perovskite surface or distorted PbI_6^{2-} octahedron, resulting in the ineffectiveness of defect passivation and perhaps causing even more defects through lattice distortion (fig. S3).

The surface passivation effects of the three molecules with different configuration were further studied by photoluminescence (PL). The PL intensity increased noticeably with the treatment by theophylline (Fig. 2D), implying the suppressed nonradiative charge-recombination sites from defects (*15*). With

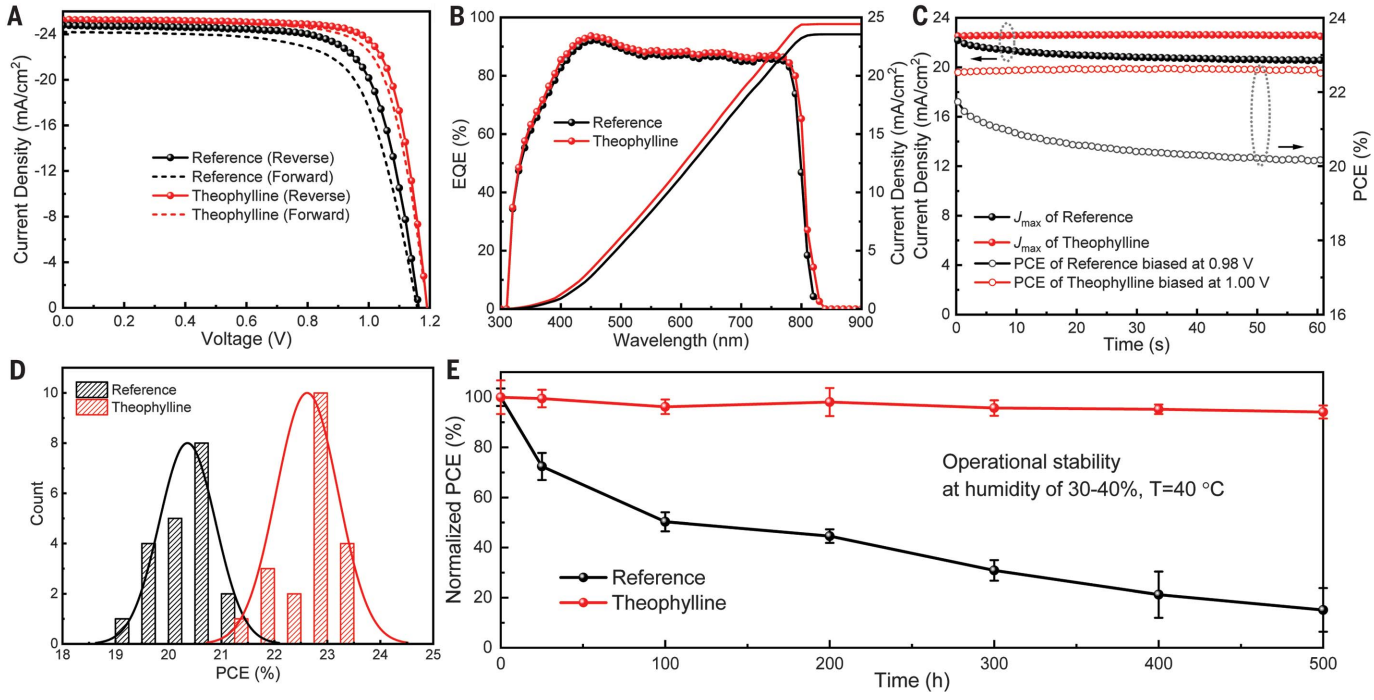

Fig. 4. Enhanced photovoltaic performance and long-term stability of perovskite solar cells with theophylline treatment. (**A**) *J-V* curves of perovskite solar cells with or without theophylline treatment. (**B**) EQE curves of perovskite solar cells with or without theophylline treatment. (**C**) Stabilized maximum power output and the photocurrent density at maximum power point as a function of time for the best-performing perovskite solar cells with or without theophylline treatment, as shown in (A), recorded under simulated 1-sun AM1.5G illumination. (**D**) PCE distribution of perovskite solar cells with or without theophylline treatment. (**E**) Evolution of the PCEs measured from the encapsulated perovskite solar cells with or without theophylline treatment exposed to continuous light (90 ± 10 mW cm^{-2}) under open-circuit condition.

the caffeine treatment, enhanced PL intensity was also observed, but not as strong as that with the theophylline, suggesting a less effective passivation effect. For theobromine, however, a decrease in PL intensity was observed compared with the reference material, which can be attributed to the destructive molecular configuration of the passivation agents causing more charge recombination sites.

The trap density of states (*t*DOS) of the as-fabricated devices were also deduced from the angular frequency-dependent capacitance. As shown in Fig. 2E, the *t*DOS as a function of the defect energy demonstrated a reduction in trap states for theophylline- and caffeine-treated perovskite compared with the reference device. By contrast, theobromine treatment induced more trap states, consistent with the decrease in PCE. The change in *t*DOS with different surface treatments was also confirmed by theoretical modeling (fig. S4). In addition, electrochemical impedance spectroscopy (EIS) characterization was performed to demonstrate the carrier transport processes under illumination at the interface. The middle frequency zone of the EIS semicircle should be dominated by junction capacitance and recombination resistance related to the interfaces between transport materials and perovskite. According to Fig. 2F, the device with theophylline surface treatment has the smallest impedance, signifying a substantially suppressed charge recombination at the interface, which originated from the reduced surface-defect states. A larger impedance was observed in caffeine-treated device, and an even larger impedance was measured in theobromine-treated device.

Further characterizations were performed to better understand the perovskite interface with theophylline. High-resolution XPS patterns of the Pb 4f for the theophylline-treated film showed two main peaks located at 138.48 and 143.38 eV, corresponding to the Pb 4f 7/2 and Pb 4f 5/2, respectively (Fig. 3A), whereas the reference film showed two main peaks at 138.27 and 143.13 eV. The peaks from Pb 4f shifted to higher binding energies in the film with theophylline surface treatment, indicating the interaction between the theophylline and the Pb on perovskite surface. We used ultraviolet photoelectron spectroscopy (UPS) to measure the surface band structure with and without the theophylline surface treatment. The work function was determined to be −4.77 and −4.96 eV with the valance band maximum of −5.66 and −5.73 eV for reference and theophylline, respectively (Fig. 3B). This difference indicated a less *n*-type surface after theophylline treatment, which could improve the hole extraction in devices.

Atomic force microscopy (AFM) combined with Kelvin probe force microscopy (KPFM) was further applied to probe the effect of theophylline on the surface morphology and surface potential. The theophylline-treated surface exhibited a higher electronic chemical potential than that of reference film, while keeping the surface morphology unchanged (Fig. 3C). The transient PL of the perovskite films with hole-transporting layer (HTL) was compared in Fig. 3D to delineate the carrier dynamics of the devices. The perovskite film with theophylline treatment showed a slightly longer carrier lifetime than the reference film, whereas a faster decay profile was observed when adding the HTL on top of the perovskite film. This result demonstrated a better hole extraction with theophylline treatment (*20*), most likely arising from lesser recombination sites at the interface and the slightly shallower work function of the perovskite film with theophylline.

The improved carrier dynamics originating from the effective surface passivation by theophylline was further characterized by cross-sectional electron-beam–induced current (EBIC) measurement. In EBIC measurement,

the electron-beam–excited carriers were collected on the basis of the collection probability CP (x, L_d), where x is the distance between junction and incident beam position, and L_d is the diffusion length of the carriers (fig. S5). The device with theophylline treatment exhibited higher EBIC current compared with the reference device (Fig. 3E). The average intensity extracted from these EBIC maps demonstrated a general increase in the EBIC signal after treatment with theophylline (fig. S6), indicating an enhanced carrier collection efficiency (*25*). Specifically, in Fig. 3E, a representative EBIC line profile of the reference device showed a current decay from the HTL-perovskite to the SnO_2-perovskite interface. The decay indicates that carrier collection was limited by the hole-diffusion length as the beam position moved away from the HTL-perovskite interface. By contrast, the device with theophylline treatment displays minimal decay in the perovskite layer in the EBIC line profile. This difference suggests that a longer diffusion length of holes was present in theophylline-treated sample and balanced electron and that hole charge transport and collection was achieved, which is likely the result of fewer surface recombination sites (Fig. 3E).

Further assessment of the performance of the PV devices based on the theophylline surface passivation was performed. The devices showed a negligible hysteresis (4.1%) (Fig. 4A) because of the balanced charge collection originating from the effective surface passivation, whereas the reference device showed a large hysteresis (up to 7.6%) (table S3). External quantum efficiency (EQE) spectra of the devices were compared in Fig. 4B. An integrated J_{SC} of 24.42 mA cm^{-2} from the target device matched well with the value measured from the *J-V* scan (<5% discrepancy), whereas the control device showed an integrated J_{SC} of 23.56 mA cm^{-2}. A stabilized PCE of 22.64% was achieved with the target device when biased at 1.00 V, whereas that of the control device was 20.36% when biased at 0.98 V (Fig. 4C). The histogram of PV efficiencies for 40 devices is shown in Fig. 4D (the detailed parameters are shown in table S2), which confirms good reproducibility of the performance improvement with theophylline (11.1% improvement in an average PCE from 20.36 ± 0.53% to 22.61 ± 0.58% with the incorporation of the theophylline).

The changes in PCE of the encapsulated devices at a relative humidity of 30 to 40% and temperature of 40°C were tracked over time to test the long-term operational stability (Fig. 4E). The reference device (initial PCE 19.34%) degraded by more than 80% in 500 hours, whereas the target device maintained >90% of its initial efficiency (21.32%) during this time. Also, as shown in fig. S7, the shelf stability of the device based on theophylline treatment was noticeably enhanced, maintaining >95% of its original PCE (22.78%) when stored under ambient conditions with 20 to 30% humidity at 25°C for 60 days. By contrast, the reference device lost >35% of its initial efficiency (20.67%). The strong interaction between the theophylline and the surface defects likely suppressed deleterious ion migration (*26*–*28*).

REFERENCES AND NOTES

1. J. Tong *et al*., *Science* **364**, 475–479 (2019).
2. H. Tan *et al*., *Science* **355**, 722–726 (2017).
3. X. Zheng *et al*., *Nat. Energy* **2**, 17102 (2017).
4. J. J. Yoo *et al*., *Energy Environ. Sci.* **12**, 2192–2199 (2019).
5. Q. Jiang *et al*., *Nat. Photonics* **13**, 460–466 (2019).
6. N. Li *et al*., *Nat. Energy* **4**, 408–415 (2019).
7. J. S. Manser, J. A. Christians, P. V. Kamat, *Chem. Rev.* **116**, 12956–13008 (2016).
8. H. Zhang *et al*., *ACS Appl. Mater. Interfaces* **10**, 42436–42443 (2018).
9. J. W. Lee, H. S. Kim, N. G. Park, *Acc. Chem. Res.* **49**, 311–319 (2016).
10. Y. Zong *et al*., *Chem* **4**, 1404–1415 (2018).
11. D. Bi *et al*., *Nat. Energy* **1**, 16142 (2016).
12. B. Chen, P. N. Rudd, S. Yang, Y. Yuan, J. Huang, *Chem. Soc. Rev.* **48**, 3842–3867 (2019).
13. T. Wu *et al*., *Adv. Energy Mater.* **9**, 1803766 (2019).
14. T. Niu *et al*., *Adv. Mater.* **30**, e1706576 (2018).
15. R. Wang *et al*., *Joule* **3**, 1464–1477 (2019).
16. W. Xu *et al*., *Nat. Photonics* **13**, 418–424 (2019).
17. H. Zhang, M. K. Nazeeruddin, W. C. H. Choy, *Adv. Mater.* **31**, e1805702 (2019).
18. W. J. Yin, T. Shi, Y. Yan, *Appl. Phys. Lett.* **104**, 063903 (2014).
19. W. S. Yang *et al*., *Science* **356**, 1376–1379 (2017).
20. N. J. Jeon *et al*., *Nat. Energy* **3**, 682–689 (2018).
21. E. H. Jung *et al*., *Nature* **567**, 511–515 (2019).
22. M. A. Green, A. Ho-Baillie, H. J. Snaith, *Nat. Photonics* **8**, 506–514 (2014).
23. Z. Xiao, Z. Song, Y. Yan, *Adv. Mater.* **31**, e1803792 (2019).
24. N. Liu, C. Yam, *Phys. Chem. Chem. Phys.* **20**, 6800–6804 (2018).
25. E. Edri *et al*., *Nat. Commun.* **5**, 3461 (2014).
26. R. Wang *et al*., *Adv. Funct. Mater.* **29**, 1808843 (2019).
27. J. A. Christians *et al*., *Nat. Energy* **3**, 68–74 (2018).
28. Y. Hou *et al*., *Science* **358**, 1192–1197 (2017).

ACKNOWLEDGEMENTS

Funding: Y.Y. acknowledges the Office of Naval Research (ONR) (N00014-17-1-2,484) for their financial support. Part of this material is based upon work supported by the U.S. Department of Energy's Office of Energy Efficiency and Renewable Energy (EERE) under the Solar Energy Technologies Office Award Number DE- EE0008751. Z.-K.W. acknowledges the Natural Science Foundation of China (no. 91733301). This project was also supported by the Collaborative Innovation Center of Suzhou Nano Science and Technology. Y.L. and D.F. are grateful for the financial support of a California Energy Commission Advance Breakthrough award (EPC-16-050). This work was performed in part at the San Diego Nanotechnology Infrastructure (SDNI) of UCSD supported by the National Science Foundation (grant ECCS-1542148). Part of the computations were performed in the SIMULAB of Marmara University, Physics Department and in the UHEM cluster of Turkey. K.N.H. and S.N. are grateful to the National Science Foundation (CHE-1764328) for financial support of this research. Computer time was provided by the UCLA Institute for Digital Research and Education (IDRE).
Author contributions: R.W., J.X., and Y.Y. conceived the idea for the study. R.W. and J.X. fabricated the solar cell devices and designed the experiments. K.-L.W. performed the film and device characterizations under the supervision of Z.-K.W. Y.L. and D.F. performed the EBIC measurement. G.X. carried out the *t*DOS measurement. S.N., I.Y., and K.N.H. performed the DFT calculation. T.H. carried out the TPC and TPV measurement. Y.Z., J.L.Y., J.Z., M.W., and S.T. assisted with the device fabrication and characterizations. R.W., J.X., and Y.Y. wrote the manuscript. All authors discussed the results and commented on the manuscript. Y.Y. supervised the project. **Competing interests:** None declared.
Data and materials availability: All (other) data needed to evaluate the conclusions in the paper are present in the paper or the supplementary materials.

SUPPLEMENTARY MATERIALS

science.sciencemag.org/content/366/6472/1509/suppl/DC1
Materials and Methods
Supplementary Text
Figs. S1 to S13
Tables S1 to S3
References (*29*–*41*)

1 August 2019; accepted 8 November 2019
10.1126/science.aay9698

Constructive molecular configurations for surface-defect passivation of perovskite photovoltaics

Rui Wang, Jingjing Xue, Kai-Li Wang, Zhao-Kui Wang, Yanqi Luo, David Fenning, Guangwei Xu, Selbi Nuryyeva, Tianyi Huang, Yepin Zhao, Jonathan Lee Yang, Jiahui Zhu, Minhuan Wang, Shaun Tan, Ilhan Yavuz, Kendall N. Houk and Yang Yang

Science **366** (6472), 1509-1513.
DOI: 10.1126/science.aay9698

Optimizing surface passivation

Unproductive charge recombination at surface defects can limit the efficiency of hybrid perovskite solar cells, but these defects can be passivated by the binding of small molecules. Wang *et al.* studied three such small molecules—theophylline, caffeine, and theobromine—that bear both carbonyl and amino groups. For theophylline, hydrogen bonding of the amino hydrogen to surface iodide optimized the carbonyl interaction with a lead antisite defect and improved the efficiency of a perovskite cell from 21 to 22.6%.

Science, this issue p. 1509